Molecular engineering binuclear copper catalysts for selective CO_2 reduction to C_2 products

Qi Zhao [a], Kai Lei [b], Bao Yu Xia [b,*], Rachel Crespo-Otero [c,*], Devis Di Tommaso [a,d,*]

[a] Department of Chemistry, School of Physical and Chemical Sciences, Queen Mary University of London, London, E1 4NS, UK
[b] Key Laboratory of Material Chemistry for Energy Conversion and Storage (Ministry of Education), Hubei Key Laboratory of Material Chemistry and Service Failure, State Key Laboratory of Materials Processing and Die & Mould Technology, School of Chemistry and Chemical Engineering, Huazhong University of Science and Technology (HUST), Wuhan 430074, Hubei, China
[c] Department of Chemistry, University College London, London, WC1H 0AJ, UK
[d] Digital Environment Research Institute, Queen Mary University of London, Empire House, London E1 1HH, UK

ARTICLE INFO

ABSTRACT

Molecular copper catalysts serve as exemplary models for correlating the structure-reaction-mechanism relationship in the electrochemical CO_2 reduction (eCO_2R), owing to their adaptable environments surrounding the copper metal centres. This investigation, employing density functional theory calculations, focuses on a novel family of binuclear Cu molecular catalysts. The modulation of their coordination configuration through the introduction of organic groups aims to assess their efficacy in converting CO_2 to C_2 products. Our findings highlight the crucial role of chemical valence state in shaping the characteristics of binuclear Cu catalysts, consequently influencing the eCO_2R behaviour. Notably, the Cu(II)Cu(II) macrocycle catalyst exhibits enhanced suppression of the hydrogen evolution reaction (HER), facilitating proton transfer and the eCO_2R process. Furthermore, we explore the impact of diverse electron-withdrawing and electron-donating groups coordinated to the macrocycle (R = –F, –H, and –OCH_3) on the electron distribution in the molecular catalysts. Strategic placement of –OCH_3 groups in the macrocycles leads to a favourable oxidation state of the Cu centres and subsequent C–C coupling to form C_2 products. This research provides fundamental insights into the design and optimization of binuclear Cu molecular catalysts for the electrochemical conversion of CO_2 to value-added C_2 products.

© 2024 Science Press and Dalian Institute of Chemical Physics, Chinese Academy of Sciences. Published by ELSEVIER B.V. and Science Press. This is an open access article under the CC BY license (http://creativecommons.org/licenses/by/4.0/).

1. Introduction

CO$_2$ conversion into high-value chemicals, fuels, and materials is a topic of significant societal and scientific importance due to its potential to alleviate the impacts of climate change and promote sustainable energy utilization [1–3]. Electrochemical carbon dioxide reduction (eCO_2R) is regarded as a promising strategy due to considerations of technical complexity, maturity, and economic feasibility, thus drawing considerable research interest from both academia and industry [4–8]. The electrocatalytic conversion of CO_2 to multi-carbon (C_{2+}) products is the holy grail of electrochemical synthesis [9–11]. Compared to one-carbon (C_1) products such as carbon monoxide (CO), methane (CH_4), formic acid ($HCOOH$), and methanol (CH_3OH), C_{2+} products like ethylene (CH_2CH_2), ethanol (CH_3CH_2OH), acetic acid (CH_3COOH), and n-propanol ($CH_3CH_2CH_2OH$) exhibit superior energy densities and economic value. Additionally, they can be utilized as feedstocks for the synthesis of long-chain hydrocarbon fuels [12–14]. Nevertheless, the pursuit of efficient catalysts that can achieve high product selectivity, particularly C_{2+} molecules, remains one of the critical technological hurdles for effective eCO_2R [15,16].

Copper (Cu) is recognized as catalytic candidates for multiple proton-coupled electron transfer (PCET) reactions to generate valuable chemicals [6,17–21]. However, most reported heterogeneous Cu catalysts (including alloys [22,23], metal oxides [24,25], nanoparticles [26,27]) often exhibit inconsistent and difficult-to-tune active sites, such as edges, corners, and facets, leading to variations in reactivity and selectivity. Moreover, the concealed Cu atoms within the bulk structure will limit atomic utilization to CO_2 reduction. Compared with traditional copper bulk catalysts, single-site molecular catalysts achieve high atomic utilization and allow for precise tuning of the active sites. By substituting

* Corresponding authors.
   E-mail addresses: byxia@hust.edu.cn (B.Y. Xia), r.crespo-otero@ucl.ac.uk (R. Crespo-Otero), d.ditommaso@qmul.ac.uk (D. Di Tommaso).

different central metals and surrounding ligands, the catalytic performance of molecular catalysts can be finely tuned to optimize the selectivity of the eCO_2R towards specific products [28,29].

In recent times, bimetallic molecular catalysts have emerged as new paradigm in the field of electrocatalysis [30,31]. Several investigations have indicated that binuclear metal catalysts exhibit superior selectivity and catalytic activity compared to mononuclear metal catalysts. This is attributed to the synergistic effects between the two metal sites, leading to a reduction in overpotential, an increase in reactivity measured by turnover number and turnover frequency, and an enhancement in product selectivity [32–39]. Recent efforts have delved into the developments in electrocatalytic reduction of CO_2 using earth-abundant bimetallic complexes, encompassing metals including Fe [40–42], Co [43], Ni [44], and Cu [45,46]. However, for the Cu-family molecule catalyst, most studies conducted thus far have concentrated on heteronuclear copper-based systems [47–49], with few exploring the performance of Cu–Cu dual sites in eCO_2R. Furthermore, there remains a gap in achieving molecular engineering to enhance the performance of bimetallic catalysts and acquiring a more profound understanding of their electrocatalytic mechanism of CO_2 reduction.

In this work, we employed computational methods based on density functional theory (DFT) to investigate the electrocatalytic conversion of CO_2 into C_1 to C_2 products using a series of binuclear CuCu macrocycle (Mac) catalysts adorned with various organic groups. By incorporating donor–acceptor groups onto the molecular macrocycle, we effectively adjusted the electron density distribution of the catalytic centre. This adjustment not only improved the control of electron distribution but also facilitated the electron migration towards CO_2 activation [29], consequently refining the selectivity of the resulting products. This study sheds lights on the influence of the $Cu^{\delta+}$ valence state on the eCO_2R process and the impact of organic groups on the electronic properties of the central Cu atoms. Our objective is to advance the rational design of molecular catalysts containing two copper atoms, with the aim of enhancing their performance in eCO_2R, especially in the generation of C_2 products.

2. Experimental

2.1. Computational details

All DFT calculations were performed using the Gaussian 16 program [50]. The Becke-type three-parameter Lee–Yang–Parr B3LYP [51] exchange correlation functional used together with the Los Alamos National Laboratory 2 double-ζ (LANL2DZ) [52] pseudopotential and basis set were used for structure optimization and frequency analysis. The B3LYP/LANL2DZ level of theory has been widely used to study the reactions of transition metal complexes [53,54]. The energies of the intermediates of the eCO_2R were refined using the correlation-consistent polarized triple-zeta (cc-pVTZ). Solvent effects were incorporated with the continuum solvation model based on density (SMD) to describe the aqueous environment. The transition state (TS) structures for the C–C coupling step were located using the QST2 option in Gaussian. Frequency calculations were then conducted to verify the TS character of located structure.

To analyse the stability of CuCu-Mac structures, we computed the formation energy (E_f) according to the following expression [55,56]:

$$E_f = \left(E_{CuCu-Mac} - E_{vo-Mac} - \frac{E_{Cu(bulk)}}{N} \right) \tag{1}$$

where the $E_{M/Mac}$ is the energy of M/Mac, N_M, N_C, and N_N are the number of metal, carbon, and nitrogen atoms in the unit cell, respectively, and μ_M, μ_C, and μ_N are the chemical potentials of the metal, carbon, and nitrogen atoms, which were obtained from the energy calculation of transition metal single atom, graphene ($\mu_C = E(Mac)/N_C$), and N_2 ($\mu_N = E(N_2)/2$), respectively. The electrochemical stability of the catalyst was evaluated by computing the dissolution potential (U_{diss}) of the metal [57]. The dissolution potential of Cu was computed according to the following expression [58].

$$U_{diss}(Cu) = U^o_{diss}(Cu, bulk) - \frac{\left(E_{CuCu-Mac} - E_{vo-Mac} - \frac{E_{Cu(bulk)}}{N} \right)}{ne} \tag{2}$$

where the values of $U^o_{diss}(Cu, bulk)$ were taken from Guo et al. [56]. and n was set to 2.

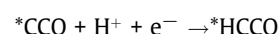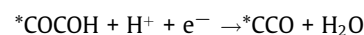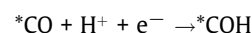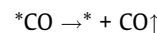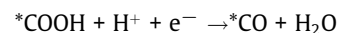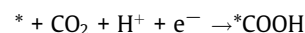The solution-phase Gibbs free energies (G) of high- and low-spin forms of all intermediates were calculated according to the following expression:
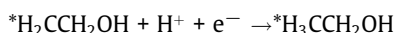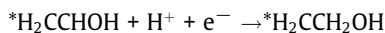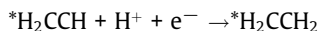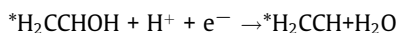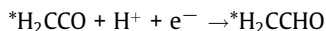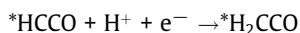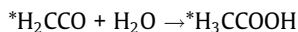
$$G = E_e + \delta G_{VRT} + \Delta G_{solv} \tag{3}$$

where the first term is the total DFT electronic energy of the intermediate, the second term is the vibrational−rotational−translational contribution to the gas-phase Gibbs free energy (δG_{VRT}) at $T = 298$ K under a standard-state partial pressure of 1 atm, and the third term is the solvation free energy corrections computed using the SMD model. The effect of pH and electrode potential (U) was then included according to the following equation for the reaction free energy (ΔG) [59]:

$$\Delta G = \Delta E_e + \Delta \delta G_{VRT} + \Delta \Delta G_{solv} + \Delta G_{pH} + \Delta G_U \tag{4}$$

where the fourth term is the free energy correction due to the difference in proton concentration, $\Delta G_{pH} = 2.303 \cdot k_B \cdot T \cdot pH$, and the last term is free energy correction due to the difference in electrode potential, $\Delta G_U = -eU$, where n is the number of electrons transferred, e is the electronic charge, and U is the applied potential. The PCET involved in the eCO_2R were studied in the framework of the Nørskov's computational hydrogen electrode (CHE) model [60]. This model provides an efficient approach to study PCET without treating solvated protons explicitly and is widely used in theoretical study of electrocatalysis. In the CHE model, zero voltage was defined based on the potential energy (μ) of components involved in the reversible hydrogen electrode at all pH, T, and p. Therefore, $\mu(H^+) + \mu(e^-) = 1/2 \ \mu(H_2)$ at a potential of 0 V. The limiting potential U_L, an important parameter for evaluating the catalytic activity, was obtained according to the formula $U_L = -\Delta G_{max}/ne$, where ΔG_{max} is the Gibbs free energy change of the rate-determining step. This methodology was used to compute the ΔG of the elementary reactions involved in the formation of the C_2 products CH_3COOH, CH_3CH_2OH, and CH_2CH_2:

$* + CO_2 + H^+ + e^- \rightarrow *COOH$

$*COOH + H^+ + e^- \rightarrow *CO + H_2O$

$*CO \rightarrow * + CO\uparrow$

$*CO + H^+ + e^- \rightarrow *COH$

$*CO + *COH \rightarrow *COCOH$

$*COCOH + H^+ + e^- \rightarrow *CCO + H_2O$

$*CCO + H^+ + e^- \rightarrow *HCCO$

$$*H_2CCO + H_2O \rightarrow *H_3CCOOH$$

$$*HCCO + H^+ + e^- \rightarrow *H_2CCO$$

$$*H_2CCO + H^+ + e^- \rightarrow *H_2CCHO$$

$$*H_2CCHO + H^+ + e^- \rightarrow *H_2CCHOH$$

$$*H_2CCHOH + H^+ + e^- \rightarrow *H_2CCH+H_2O$$

$$*H_2CCH + H^+ + e^- \rightarrow *H_2CCH_2$$

$$*H_2CCHOH + H^+ + e^- \rightarrow *H_2CCH_2OH$$

$$*H_2CCH_2OH + H^+ + e^- \rightarrow *H_3CCH_2OH$$
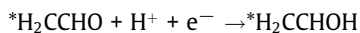
2.2. Computational models

The binuclear Cu macrocycles investigated in this study, denoted as [CuCu-Mac-n], are depicted in Fig. 1. Their design takes inspiration from the work of Yamasumi et al. [61]. Here, we explore the use of small organic ligands with n representing various substituents (n = F, CH$_3$, 2OCH$_3$, 4OCH$_3$, and 6OCH$_3$) to modulate the binuclear Cu electronic state at the centre and enhance the catalytic performance for eCO$_2$R. The interatomic distances (d) between the central Cu atoms, which are reported in Table S1, reveal that d[Cu(I)-Cu(I)] is 2.817 Å and d[Cu(II)-Cu(II)] is 2.988 Å. Out-of-plane distortions observed in [Cu(I)Cu(I)]-Mac and [Cu(II)Cu(I)]-Mac are significantly reduced in [Cu(II)Cu(II)]-Mac, as depicted in Figs. S1 and S2 of the Supporting Information (SI). This closer approach to planarity could potentially influence its catalytic activity. In a previous DFT study by Cove et al. [44], changes in planarity were also observed for metal porphyrins catalysts.

As detailed in Table S2, the formation energies of metal coordination into nitron-oxygen atoms in Mac structures are as follows: −6.81 eV in CuCu-Mac, −6.86 eV in [CuCu-Mac]–2OCH$_3$, −6.76 eV in [CuCu-Mac]-4OCH$_3$, and −6.80 eV in [CuCu-Mac]-6OCH$_3$. These values, being highly negative, indicate the stability of the complexes. Additionally, examining the dissolution potential values presented in Table S2, all catalysts exhibit U_{diss} values more positive than the experimentally applied potential for eCO$_2$R (ranging from −0.2 to 1.2 V) [58]. This suggests that the active sites are stable and resistant to dissolution during eCO$_2$R.

3. Results and discussion

3.1. The effect of the oxidation state of the $Cu^{\delta+}$ centre on the eCO$_2$R reactivity

The oxidation state of the metal centre in the molecular catalyst significantly influences the energetics of the eCO$_2$R to CO, as reported by Cove et al. [44]. Moreover, recently, Liu et al. investigated the binuclear Cu(II) macrocycle compound for selective reduction of CO$_2$ to ethylene [62]. We have conducted a comparative analysis of the catalytic behaviour of binuclear macrocycles containing Cu centres with varying chemical valence states, including [Cu(I)Cu(I)-Mac], [Cu(II)Cu(I)-Mac], and [Cu(II)Cu(II)-Mac], as shown in Fig. 2. The Gibbs free energy diagram in Fig. 2(a) reveals that the reaction free energy (ΔG) of CO$_2$ adsorption (* + CO$_2$ → *CO$_2$) is 1.77 eV on [Cu(II)Cu(I)-Mac], indicating a distinctive CO$_2$ molecule adsorption mechanism on such mix valence state, which will be delved deeper into the intricacies of this phenomenon in the subsequent analysis. On the other hand, the ΔG values of CO$_2$ adsorption on [Cu(II)Cu(II)-Mac] (0.41 eV) and [Cu(I)Cu(I)-Mac] (0.24 eV) are similar. Following CO$_2$ adsorption, the initial PCET step, leading to the formation of formate (*CO$_2$ + H$^+$ + e$^-$ → *COOH) is pivotal in generating the crucial *CO intermediate.

To quantify the selectivity of binuclear Cu catalysts towards CO$_2$ reduction over HER, we employed the difference between the limiting potential of the eCO$_2$R, U_L(CO$_2$R), as shown in Fig. 2(a), and the HER, U_L(HER), as shown in Fig. 2(b) [21]. This difference is denoted as $\Delta U_L = U_L$(CO$_2$R) − U_L(HER). The limiting potential refers to the minimum reverse electrode potential required to overcome the PCET step associated with the largest positive free
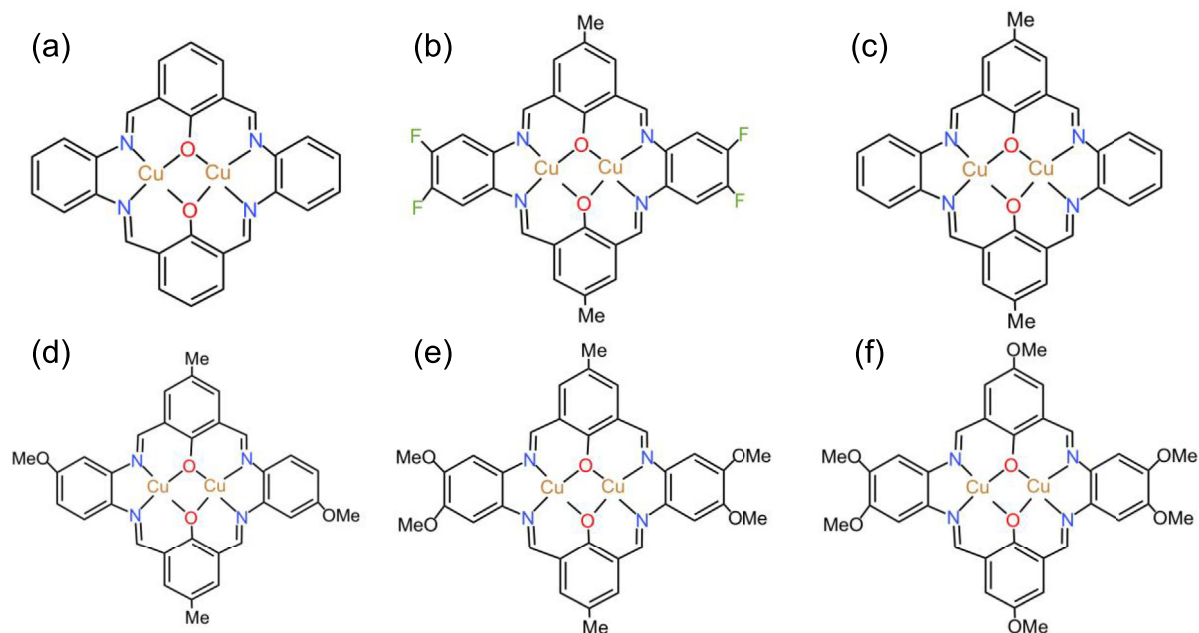

Fig. 1. The binuclear Cu macrocycles [CuCu-Mac-n] considered in this study: (a) [CuCu-Mac]; (b) [CuCu-Mac-F]; (c) [CuCu-Mac-CH$_3$]; (d) [CuCu-Mac-2OCH$_3$]; (e) [CuCu-Mac-4OCH$_3$]; (f) [CuCu-Mac-6OCH$_3$].
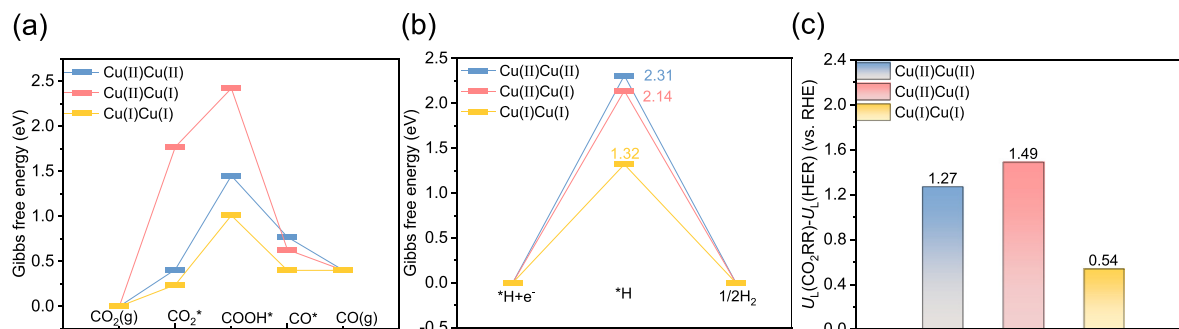
Fig. 2. Gibbs free energy diagrams of the (a) CO_2 reduction reaction and (b) hydrogen evolution reaction. (c) The values of $\Delta U_L = U_L(CO_2RR) - U_L(HER)$ on the binuclear Cu macrocycle with varying valence oxidation state of the Cu centres: [Cu(I)Cu(I)-Mac]; [Cu(II)Cu(I)-Mac]; [Cu(II)Cu(II)-Mac].

energy change in the reaction pathway. Consequently, a positive ΔU_L indicates that the largest Gibbs free energy step during eCO_2R is smaller than that of HER, resulting in a greater selectivity for CO_2 reduction over hydrogen evolution [21,63,64]. The computed ΔU_L values for the eCO_2R to CO on [Cu(I)Cu(I)-Mac], [Cu(II)Cu(I)-Mac], and [Cu(II)Cu(II)-Mac] are summarized in Fig. 2(c). Notably, on [Cu(II)Cu(II)-Mac], the upper limit potential (ΔU_L) reaches 1.27 V, significantly exceeding the value of 0.54 V observed on [Cu(I)Cu(I)-Mac]. This divergence in ΔU_L values aligns with the HER hinderance observed on [Cu(II)Cu(II)-Mac]. On [Cu(II)Cu(II)-Mac], the *CO desorption energy is −0.37 eV, whereas on [Cu(I)Cu(I)-Mac], it is close to 0 eV, indicating a competitive reaction between *CO desorption and further *CO reduction on [Cu(II)Cu(II)-Mac]. From the geometric features listed in Table S1 corresponding to Fig. 1, the low valence state Cu(I) brings the binuclear Cu atoms into proximity, a spatial arrangement that induces a stronger interaction between the two Cu atoms.

We employed frontier molecular orbitals (MOs) to elucidate the differences in CO_2 binding strength with the chemical valence state of the binuclear Cu complexes. The frontier MOs encompass the highest occupied molecular orbital (HOMO) and the lowest unoccupied molecular orbital (LUMO). For the isolated CO_2 molecule, the HOMO and LUMO levels are located at −10.18 and 0.35 eV (Fig. S3). Muthuperiyanayagam et al. reported that CO_2 activation results from electronic charge transfer between the HOMO of the metal catalyst and the LUMO of the CO_2 molecule [59]. In this study, the HOMO of [Cu(I)Cu(I)-Mac] is −4.14 eV, closer to the LUMO of the CO_2 molecule (0.35 eV) than the HOMO (−11.46 eV) of [Cu(II)Cu(II)-Mac]. Therefore, the Cu(I) centre could be more stable during the CO_2 activation process. The HOMO-LUMO electronic density distribution in Fig. S4 shows [Cu(I)Cu(I)-Mac] has a more delocalized feature than [Cu(II)Cu(II)-Mac], which further confirms the activity of [Cu(I)Cu(I)-Mac]. Moreover, Fig. S4 reveals a significantly reduced HOMO-LUMO gap (1.20 eV) for [Cu(II)Cu(I)-Mac] compared to both [Cu(II)Cu(II)-Mac] (1.72 eV) and [Cu(I)Cu(I)-Mac] (1.85 eV), suggesting a potentially easier electron excitation in the mixed-valence complex. This aligns with the higher degree of charge transfer towards CO_2 in [Cu(II)Cu(I)-Mac] reported in Table S3. Interestingly, while [Cu(II)Cu(II)-Mac] and [Cu(I)Cu(I)-Mac] exhibit CO_2 physisorption (weak interaction through van der Waals forces) in Fig. S9(a and h), respectively, [Cu(II)Cu(I)-Mac] in Fig. S9(e) shows chemisorption. This suggests a different adsorption mechanism for the mixed-valence state. In other computational studies on the topic of catalytic CO_2 conversion, it is frequently observed that CO_2 tends to exhibit greater stability in the physisorption state as opposed to chemisorption [63,65–68]. In terms of adsorbed geometry configuration, the predominant scenario observed in this study involves intermediates preferentially occupying the bridge sites of binuclear Cu. This

utilization of binuclear Cu capitalizes on the synergistic effect, thereby enhancing reaction efficiency, especially in the coupling of intermediates. Initial attempts were made to adsorb intermediates on the top site of a single Cu metal. However, following DFT optimization, stable geometric configurations were consistently maintained between the two Cu atoms, as illustrated in Figs. S9–S12. The free energy diagram (Fig. S7) illustrates that the C_2 pathway possesses a lower potential determining step (PDS) compared to the C_1 pathway. Specifically, as summarised in Fig. 3, the PDS for C_2 is 0.4 eV, while the PDS for C_1 is 1.29 eV. This lower PDS suggests that C_2 formation is thermodynamically favoured on the [CuCu-Mac] catalyst.

3.2. Effect of electron-withdrawing and electron-donating groups on eCO_2R

In addition to the oxidation state of the Cu atoms, we also investigated the influence of the organic functional groups on the electronic distribution around the binuclear Cu and its ability to reduce CO_2. Based the reaction Gibbs free energy change on eCO_2R (Fig. 4a) and HER (Fig. 4b), we plotted the difference between the limiting potentials, $U_L(CO_2RR)$, and the $U_L(HER)$, denoted as $\Delta U_L = U_L(CO_2R) - U_L(HER)$ (Fig. 4c). The positive ΔU_L value indicates that the largest Gibbs free energy step during the eCO_2R is smaller than the largest one during the HER, leading a greater selectivity for carbon products over H_2 formation [21]. It is noted that in Fig. 4(c), the performance does not show a consistent trend as the number of OCH_3 groups increases, which may be related to the spatial orientation of the OCH_3 groups. Specifically, 4OCH_3 is positioned near both sides of the binuclear coppers, while 6OCH_3 has the additional two OCH_3 groups oriented perpendicular to the CuCu binuclear axis shown Fig. 1. This may lead to a more uniform distribution of electron accumulation on the binuclear Cu macrocycle, potentially buffering the catalyst function. As a result, the HOMO level does not exhibit a consistent trend in Fig. 5, ranging from −3.90 eV for 2OCH_3 to −3.70 eV for 4OCH_3, and −3.73 eV for 6OCH_3. The positive ΔU_L value indicates that the largest Gibbs free energy step during the eCO_2R is lower than that of the HER, suggesting an inhibitory effect on the competitive hydrogen evolution reaction [21]. On Cu-Mac-4(OCH_3), the ΔU_L value can reach 0.44 V, exceeding the values of 0.25 V on Cu-Mac-2(OCH_3) and 0.18 V on Cu-Mac-6(OCH_3). These findings suggest that the Cu-Mac-4(OCH_3) catalyst inhibits the HER, thus demonstrating the potential for high selectivity towards the formation of carbon intermediates.

Organic groups can stabilize the oxidation state of binuclear Cu catalyst, as exhibited in Figs. S5 and S6, and control the electron distribution around the metal centres. This regulation will further lead to improved effectiveness and specificity [44]. In Fig. 5, we illustrate the impact of electron-withdrawing and electron-
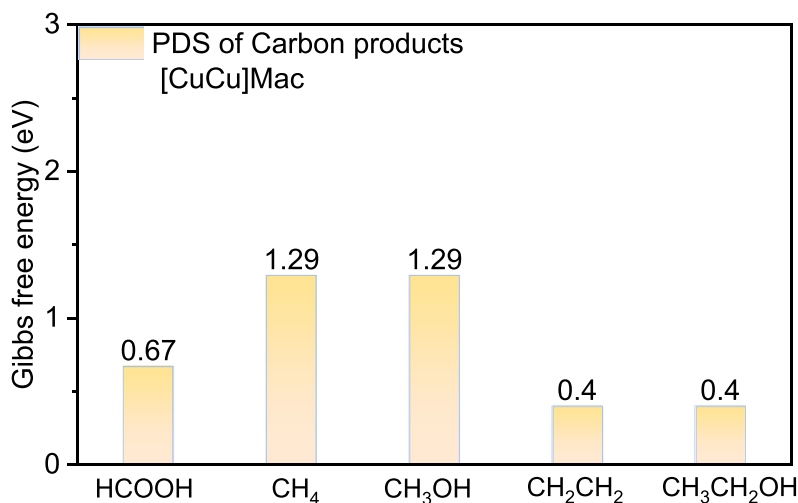
Fig. 3. Gibbs free energy values of the potential determining step (PDS) for the formation of C_1 (HCOOH, CH_4, CH_3OH) and C_2 (CH_2CH_2, CH_3CH_2OH) products on CuCu-Mac.
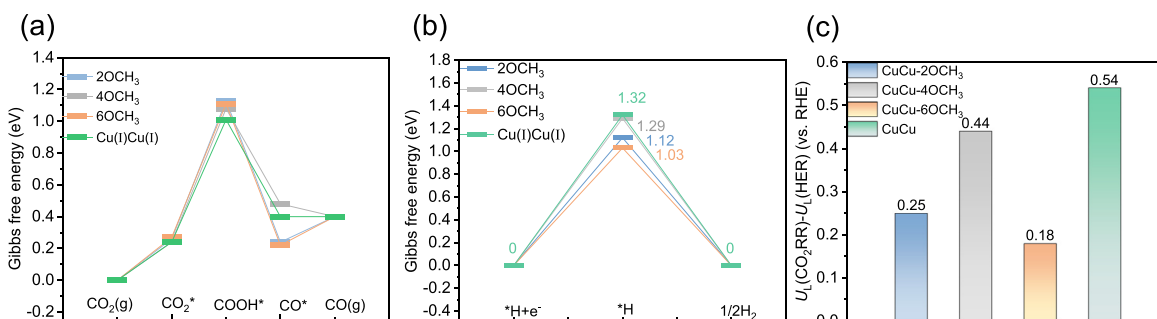
Fig. 4. Gibbs free energy diagram of (a) eCO_2R on Cu-Mac-nOCH$_3$ (n = 2, 4, 6); (b) HER on Cu-Mac-nOCH$_3$; (c) $U_L(CO_2R)$-$U_L(HER)$ on Cu-Mac-nOCH$_3$ (more positive values correspond to higher propensity for CO formation).
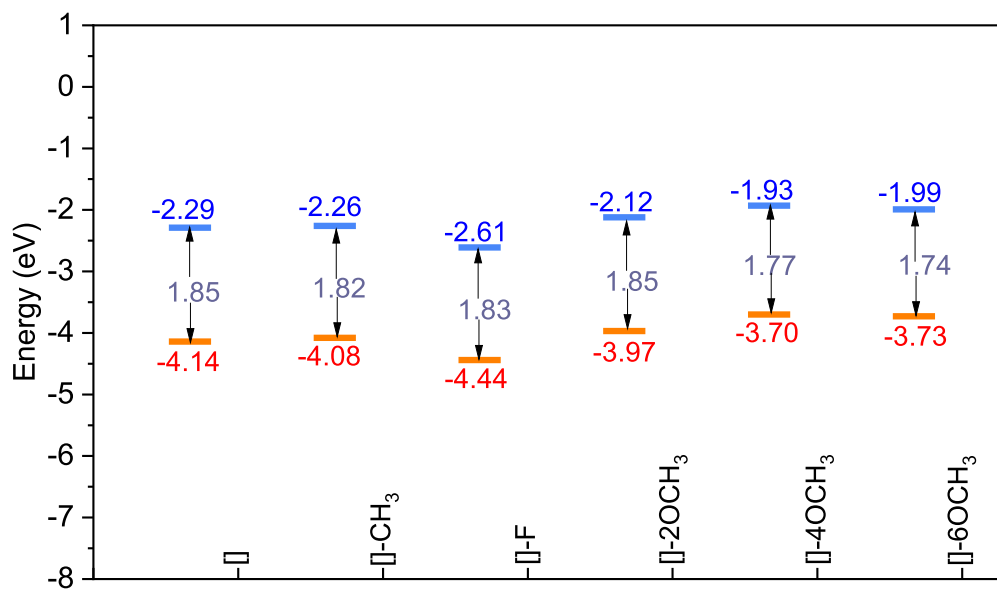

Fig. 5. The HOMO-LUMO levels in CuCu-Mac (in eV) without and with electron-withdrawing and electron-donating groups. Values obtained from DFT calculations at the B3LYP/cc-pVTZ//B3LYP/LANLDZ level of theory.

donating groups (R = –F, –H, and –OCH$_3$) on the HOMO-LUMO levels. Comparing with the bare CuCu-Mac system, the HOMO level shifts from –4.14 to –4.08 eV when R = CH$_3$, to –4.44 eV when R = F, to –3.97 eV when R = 2OCH$_3$, to –3.70 eV when R = 4OCH$_3$, and to –3.73 eV when R = 6OCH$_3$ (Fig. 5). A catalyst with a higher HOMO energy facilitates the transfer of electrons to the LUMOs of the CO$_2$ and CO molecules, promoting CO$_2$ activation, and the subsequent conversion of carbon intermediates.

Bader charge analysis (Figs. S5 and S6) reveals that organic ligands oxidize the central Cu atoms for the higher charge values. For instance, compared to the unfunctionalized [Cu$_2$-Mac] in Fig. S5(a) with a Bader charge of +0.836 and +0.841 on the two Cu atoms, both [Cu$_2$-4OCH$_3$] in Fig. S6(d) and [Cu$_2$-6OCH$_3$] in Fig. S6(e) exhibit higher charges of +0.873 and +0.863, and +0.886 and +0.883, respectively. Variation of the Bader charges of the metal centres before and after CO$_2$ adsorption reported in Table S3 reveals that –OCH$_3$ groups enhance electron density transfer onto CO$_2$. Compared to the unfunctionalized catalyst, CO$_2$ adsorbed on the Cu–Cu binuclear macrocycle with two –OCH$_3$ groups exhibits a 4.6% increase in positive charge. Introducing four –OCH$_3$ groups further increases the CO$_2$ charge by 3.3%, and to a substantial 10.6% charge enhancement with six –OCH$_3$ ligands. According to these findings, the incorporation of –OCH$_3$ groups in bimetallic [CuCu]-Mac catalysts influence the electron density in the molecular catalyst and could facilitate the reduction of the CO$_2$ molecule.

3.3. Carbon coupling reaction and formation of C$_2$ molecules

The conversion of the *CO intermediate is the initial step in the formation of C$_2$ products, including CH$_3$COOH, CH$_3$CH$_2$OH, and CH$_2$CH$_2$ [69,70]. As depicted in Fig. S7, we computed the free energies of all possible C–C coupling reactions: 2*CO → *COCO (ΔG = –3.67 eV); 2*CHO → CHOCHO* (ΔG = –3.40 eV); *COH + *CHO → CHOCOH* (ΔG = –2.29 eV); CO* + COH* → COCOH* (ΔG = –0.14 eV); CO* + CHO* → COCHO* (ΔG = 1.25 eV). The significantly

negative free energy of formation for *COCO (–3.61 eV) implies that this intermediate could be excessively stable, posing a difficulty to subsequent reduction reactions, and thus impeding the generation of C$_2$ products. Taking the coupling reaction path 2*CO → *COCO as a case, the energy required for the subsequent PCET step, *COCO + (H$^+$ + e$^-$) → COCOH in Fig. S7(d) is ΔG = 5.05 eV. Similarly, the PCET at the carbon end, *COCO + (H$^+$ + e$^-$) → COCHO in Fig. S7(d), requires an energy of ΔG = 5.92 eV. Both these steps are thermodynamically unfavourable. For the C–C coupling step and the subsequent PCET steps to take place, the reaction free energy of the C–C coupling step should be mildly exothermic. Given the previous analysis, *CO + *COH → *COCOH is the preferred coupling path with a reaction Gibbs free energy of –0.14 eV, as shown in Fig. S7(c)). Moreover, according to the computational study by Calle-Vallejo and Koper on eCO$_2$R to C$_2$ products [69], the C–C distance serves as an indicator for monitoring multiple bonds in intermediates. In the COCOH intermediate, the C–C distance of 1.50 Å suggests a more stable single bond compared to COCHO, which has a C–C bond length of 1.31 Å (Fig. 6).

Henceforth, the COCOH intermediate is considered as the key intermediate for the generation of C$_2$ products, as shown in [60,69]. Therefore, the activation barrier for the C–C coupling reaction leading to COCOH was also considered. As shown in Fig. 6, the barrier for CO-COH coupling on [CuCu]-4OCH$_3$ is 0.05 eV, while on [CuCu]-6OCH$_3$ it is 0.9 eV, and on [CuCu]-Mac without ligands, the kinetic barrier reaches as high as 0.66 eV (Fig. S7(e)). In this regard, the inclusion of –OCH$_3$ ligands decreases the carbon coupling kinetic barrier. Starting with the coupling reaction *CO + *COH → *COCOH, we computed the subsequent PCET steps responsible for the formation of CH$_3$COOH, CH$_3$CH$_2$OH, and C$_2$H$_2$ on [CuCu-Mac-nOCH$_3$] (n = 4, 6). The catalytic pathways associated with these products, along with the corresponding reaction free energy values, are presented in Fig. 6. All free energies are referenced to U = –1.25 vs. RHE (reversible hydrogen electrode) (values reported in Table S10) and the structures of the intermediates are illustrated in Figs. S11 and S12. The reaction free energies referenced to U = 0
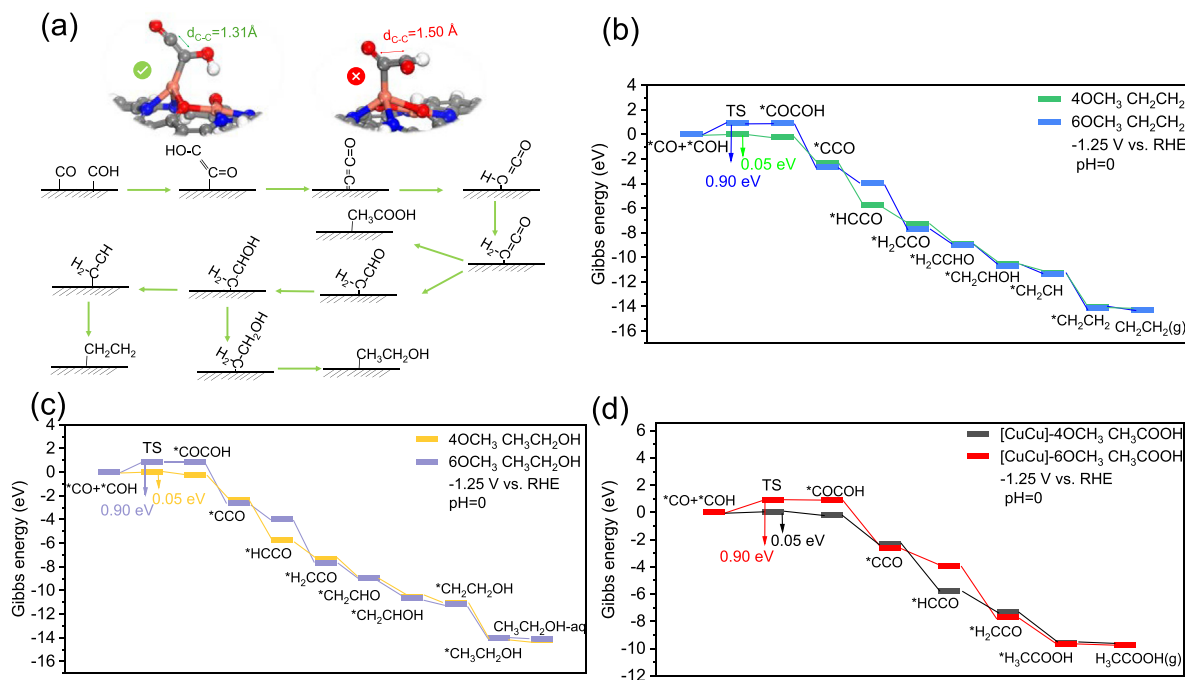

Fig. 6. (a) Lowest potential pathway towards C$_2$ products. Gibbs free energy diagrams for the formation of (b) CH$_2$CH$_2$, (c) CH$_3$CH$_2$OH, and (d) CH$_3$COOH on [CuCu]-4OCH$_3$ and [CuCu]-6OCH$_3$ at conditions of U = –1.25 vs. RHE and pH = 0.

vs. RHE are presented in Fig. S8 and Table S9. For [CuCu-Mac-4OCH$_3$], the Gibbs free energy of the *CO + *COH → *COCOH step is −0.20 eV. Coupled with a kinetic barrier of 0.05 eV and the subsequent spontaneous PCET reactions, the C$_2$ production pathways could be favourable on [CuCu]-4OCH$_3$. However, when comparing the pathways on [CuCu-Mac]-4OCH$_3$ and [CuCu-Mac]-6OCH$_3$, the key C–C coupling step (*CO + COH → COCOH) at the binuclear Cu centre experiences a slightly less favourable free energy change on [CuCu-Mac]-6OCH$_3$ (ΔG = 0.90 eV). This disadvantage in C$_2$ product formation might be attributed to the lower HOMO energy level observed after 6OCH$_3$ coordination (−3.73 eV in Fig. 5) compared to the −3.70 eV on [CuCu-Mac]-4OCH$_3$.

Fig. 6 illustrates the reaction mechanism for C$_2$ products including *CH$_2$CH$_2$, *CH$_3$CH$_2$OH, and *CH$_3$COOH formation. The *H$_2$CCO intermediate is shared between the pathways leading to CH$_2$CH$_2$ (Fig. 6b), CH$_3$CH$_2$OH (Fig. 6c), and CH$_3$COOH (Fig. 6d) [33,70]. On [CuCu]-4OCH$_3$, following the CO + COH coupling reaction, the CH$_3$COOH pathway, depicted by the black line in Fig. 6(d), involves the sequential steps COCOH → CCO → HCCO → H$_2$CCO → H$_3$CCOOH. The intermediate *H$_3$CCOOH forms through the reaction of H$_2$O with CH$_2$CO*, specifically, CH$_2$CO* + H$_2$O → *CH$_3$COOH. The final step of CH$_3$COOH desorption from the binuclear catalyst is favourable (ΔG = −0.2 eV). Prior to the formation of *CH$_3$COOH, the intermediate *H$_2$CCO engages in a competitive pathway leading to *CH$_2$CH$_2$, where the preceding step is *CH$_2$CHOH + (H$^+$ + e$^-$) → *CH$_2$CH + H$_2$O with a Gibbs reaction free energy of −0.70 eV, as illustrated by the green line in Fig. 6(b). Similarly, from the *CH$_2$CH$_2$ intermediate, *CH$_2$CHOH participates in another pathway resulting in *CH$_3$CH$_2$OH and the subsequent formation of ethanol (*CH$_2$CHOH + (H$^+$ + e$^-$) → *CH$_2$CH$_2$OH, ΔG = −0.49 eV), as shown in Fig. 6(c). Furthermore, the influence of pH on the reaction pathway is shown in Fig. S8(d–f). The pH significantly impacts the reaction pathways, lowering the Gibbs free energy of the final intermediate *CH$_2$CH$_2$. On [CuCu-4OCH$_3$], *CH$_2$CH$_2$ binding adopts a much more favorable energy state at pH = 0 (−5.34 eV, Fig. S8a) compared to pH = 7 (−4.92 eV, Fig. S8d). Similar trends are observed for the CH$_3$CH$_2$OH and CH$_3$COOH pathways, suggesting enhanced product stabilization at lower pH. Based on the above analysis, [CuCu-Mac]-4OCH$_3$ exhibits the most favourable reaction pathway to C$_2$ products.

4. Conclusions

We conducted DFT calculations of the electrochemical reduction of CO$_2$ to C$_1$ and C$_2$ products on binuclear [CuCu-Mac] molecular catalysts. Our observations revealed that the chemical valence state influences the catalytic properties of binuclear Cu macrocycles and its CO$_2$ reduction behaviour: [Cu(II)Cu(II)-Mac] exhibits greater hindrance towards the hydrogen evolution reaction; [Cu(I)Cu(I)-Mac] possesses a stronger binding affinity for *CO; mix-valence state [Cu(II)Cu(I)-Mac] exhibits a different CO$_2$ adsorption mechanism, preferring the CO$_2$ chemisorption. Furthermore, organic ligands were identified as effective modulators of the HOMO-LUMO levels of the molecular catalyst. The –OCH$_3$ group demonstrates a significant enhancement in CO$_2$ activation. Notably, the [CuCu-Mac] catalyst adorned with four –OCH$_3$ groups exhibited a decrease in the potential-limiting step of C$_2$ pathways. This study highlights the effectiveness of organic groups in fine-tuning the electronic properties of binuclear Cu macrocycle for electrocatalysis, thereby optimizing the CO$_2$ to C$_2$ reduction. In summary, this study explored the potential of binuclear [CuCu]-Mac for selectively generating value-added C$_2$ chemicals, effectively briding the gap between theoretical design and practical application.

Declaration of competing interest

The authors declare that they have no known competing financial interests or personal relationships that could have appeared to influence the work reported in this paper.

Appendix A. Supplementary material

Supplementary material to this article can be found online at https://doi.org/10.1016/j.jechem.2024.01.060.

References

[1] P. Friedlingstein, M.W. Jones, M. O'Sullivan, R.M. Andrew, D.C. Bakker, J. Hauck, C. Le Quéré, G.P. Peters, W. Peters, J. Pongratz, Earth. Syst. Sci. Data 14 (2022) 1917–2005.
[2] S. Chu, A. Majumdar, Nature. 488 (2012) 294–303.
[3] J.A. Turner, Science. 305 (2004) 972–974.
[4] J.B. Greenblatt, D.J. Miller, J.W. Ager, F.A. Houle, I.D. Sharp, Joule. 2 (2018) 381–420.
[5] S. Nitopi, E. Bertheussen, S.B. Scott, X. Liu, A.K. Engstfeld, S. Horch, B. Seger, I.E. Stephens, K. Chan, C. Hahn, Chem. Rev. 119 (2019) 7610–7672.
[6] H. Xie, T. Wang, J. Liang, Q. Li, S. Sun, Nano. Today 21 (2018) 41–54.
[7] L. Chen, C. Tang, K. Davey, Y. Zheng, Y. Jiao, S.Z. Qiao, Chem. Sci 12 (2021) 8079–8087.
[8] F.A. Rahman, M.M.A. Aziz, R. Saidur, W.A.W.A. Bakar, M. Hainin, R. Putrajaya, N.A. Hassan, Renew. Sust. Energ. Rev. 71 (2017) 112–126.
[9] X. Wang, Q. Hu, G. Li, H. Yang, C. He, Electrochem. Energy Rev. 5 (2022) 28.
[10] T. Kim, G.T.R. Palmore, Nat. Commun. 11 (2020) 3622.
[11] C. Chen, X. Yan, S. Liu, Y. Wu, Q. Wan, X. Sun, Q. Zhu, H. Liu, J. Ma, L. Zheng, Angew. Chem. 132 (2020) 16601–16606.
[12] W. Lai, Y. Qiao, J. Zhang, Z. Lin, H. Huang, Energy. Environ. Sci. 15 (2022) 3603–3629.
[13] B. Chang, H. Pang, F. Raziq, S. Wang, K.-W. Huang, J. Ye, H. Zhang, Energy. Environ. Sci. 16 (2023) 4714–4758.
[14] M. Jouny, W. Luc, F. Jiao, Nat. Catal. 1 (2018) 748–755.
[15] L. Wang, H. Chen, Y. Wang, X. Liu, C. Li, J. He, T. Yao, Nano Res. 16 (2023) 8597–8613.
[16] R.-B. Song, W. Zhu, J. Fu, Y. Chen, L. Liu, J.-R. Zhang, Y. Lin, J.-J. Zhu, Adv. Mater. 32 (2020) 1903796.
[17] K.P. Kuhl, T. Hatsukade, E.R. Cave, D.N. Abram, J. Kibsgaard, T.F. Jaramillo, J. Am. Chem. Soc. 136 (2014) 14107–14113.
[18] A.A. Peterson, F. Abild-Pedersen, F. Studt, J. Rossmeisl, J.K. Nørskov, Energy. Environ. Sci. 3 (2010) 1311–1315.
[19] K.P. Kuhl, E.R. Cave, D.N. Abram, T.F. Jaramillo, Energy. Environ. Sci. 5 (2012) 7050–7059.
[20] J. Jiao, R. Lin, S. Liu, W.C. Cheong, C. Zhang, Z. Chen, Y. Pan, J. Tang, K. Wu, S.F. Hung, H.M. Chen, L. Zheng, Q. Lu, X. Yang, B. Xu, H. Xiao, J. Li, D. Wang, Q. Peng, C. Chen, Y. Li, Nat. Chem. 11 (2019) 222–228.
[21] Q. Zhao, R. Crespo-Otero, D. Di Tommaso, J. Energy Chem. 85 (2023) 490–500.
[22] C. Kim, F. Dionigi, V. Beermann, X. Wang, T. Möller, P. Strasser, Adv. Mater. 31 (2019) 1805617.
[23] S. Shen, X. Peng, L. Song, Y. Qiu, C. Li, L. Zhuo, J. He, J. Ren, X. Liu, J. Luo, Small. 15 (2019) 1902229.
[24] X. Wang, K. Klingan, M. Klingenhof, T. Möller, J. Ferreira de Araújo, I. Martens, A. Bagger, S. Jiang, J. Rossmeisl, H. Dau, Nat. Commun. 12 (2021) 794.
[25] J.J.s. Velasco Vélez, C.H. Chuang, D. Gao, Q. Zhu, D. Ivanov, H.S. Jeon, R. Arrigo, R.V. Mom, E. Stotz, H.L. Wu, ACS. Catal. 10 (2020) 11510–11518.
[26] Z. Ma, C. Tsounis, C.Y. Toe, P.V. Kumar, B. Subhash, S. Xi, H.Y. Yang, S. Zhou, Z. Lin, K.-H. Wu, ACS. Catal. 12 (2022) 4792–4805.
[27] C. Cao, Z. Wen, J. CO2 Util. 22 (2017) 231–237.

[28] S. Ren, D. Joulié, D. Salvatore, K. Torbensen, M. Wang, M. Robert, C.P. Berlinguette, Science 365 (2019) 367–369.
[29] D.H. Nam, P. De Luna, A. Rosas-Hernández, A. Thevenon, F. Li, T. Agapie, J.C. Peters, O. Shekhah, M. Eddaoudi, E.H. Sargent, Nat. Mater. 19 (2020) 266–276.
[30] H.Q. Liang, T. Beweries, R. Francke, M. Beller, Angew. Chem. 134 (2022) e202200723.
[31] Q. An, J. Jiang, W. Cheng, H. Su, Y. Jiang, Q. Liu, Small 6 (2022) 2200408.
[32] W.K. Walker, B.M. Kay, S.A. Michaelis, D.L. Anderson, S.J. Smith, D.H. Ess, D.J. Michaelis, J. Am. Chem. Sci. 137 (2015) 7371–7378.
[33] R.B. Siedschlag, V. Bernales, K.D. Vogiatzis, N. Planas, L.J. Clouston, E. Bill, L. Gagliardi, C.C. Lu, J. Am. Chem. Sci. 137 (2015) 4638–4641.
[34] T.J. Steiman, C. Uyeda, J. Am. Chem. Sci. 137 (2015) 6104–6110.
[35] T.J. Mazzacano, N.P. Mankad, J. Am. Chem. Sci. 135 (2013) 17258–17261.
[36] S.M. Ahmed, A. Poater, M.I. Childers, P.C.B. Widger, A.M. LaPointe, E.B. Lobkovsky, G.W. Coates, L. Cavallo, J. Am. Chem. Sci. 135 (2013) 18901–18911.
[37] J.P. Collman, N.K. Devaraj, R.A. Decréau, Y. Yang, Y.-L. Yan, W. Ebina, T.A. Eberspacher, C.E.D. Chidsey, Science 315 (2007) 1565–1568.
[38] L.K.G. Ackerman, M.M. Lovell, D.J. Weix, Nature 524 (2015) 454–457.
[39] J.W. Wang, D.-C. Zhong, T.-B. Lu, Coord. Chem. Rev. 377 (2018) 225–236.
[40] C. Costentin, S. Drouet, M. Robert, J.M. Savéant, Science 338 (2012) 90–94.
[41] H. Rao, L.C. Schmidt, J. Bonin, M. Robert, Nature 548 (2017) 74–77.
[42] J. Bonin, M. Robert, M. Routier, J. Am. Chem. Sci. 136 (2014) 16768–16771.
[43] Z. Guo, G. Chen, C. Cometto, B. Ma, H. Zhao, T. Groizard, L. Chen, H. Fan, W.L. Man, S.M. Yiu, Nat. Catal. 2 (2019) 801–808.
[44] Cove, Henry, Dimitrios Toroz, Devis Di Tommaso, Mol. Catal. 498 (2020) 111248.
[45] J.S. Field, R.J. Haines, C.J. Parry, S.H. Sookraj, Polyhedron 12 (1993) 2425–2428.
[46] R.J. Haines, R.E. Wittrig, C.P. Kubiak, Inorg. Chem. 33 (1994) 4723–4728.
[47] K. Chida, T. Yoshii, N. Hiyoshi, T. Itoh, J. Maruyama, K. Kamiya, M. Inoue, F. Tani, H. Nishihara, Carbon 201 (2023) 338–346.
[48] R. Carballo, V. Campodall'Orto, I.N. Rezzano, J. Mol. Catal. A Chem. 280 (2008) 156–163.
[49] D. Zhang, P. Du, J. Liu, R. Zhang, Z. Zhang, Z. Han, J. Chen, X. Lu, Small 16 (2020) 2004679.
[50] M. Frisch, G. Trucks, H. Schlegel, G. Scuseria, M. Robb, J. Cheeseman, G. Scalmani, V. Barone, G. Petersson, H. Nakatsuji, Wallingford CT 3 (2016).

[51] P.J. Stephens, F.J. Devlin, C.F. Chabalowski, M.J. Frisch, The J. Phys. Chem. C 98 (1994) 11623–11627.
[52] P.J. Hay, W.R. Wadt, The J. Chem. Phys. 82 (1985) 270–283.
[53] H. Ezzat, A. Menazea, W. Omara, O.H. Basyouni, S.A. Helmy, A.A. Mohamed, W. Tawfik, M. Ibrahim, Biointerface Res. Appl. Chem 10 (2020) 7002–7010.
[54] E.D. Jemmis, M. Manoharan, P.K.J.O. Sharma, Organometallics 19 (2000) 1879–1887.
[55] J.H. Liu, L.M. Yang, E. Ganz, J. Mater. Chem. A 7 (2019) (1952) 11944–111941.
[56] X. Guo, J. Gu, S. Lin, S. Zhang, Z. Chen, S. Huang, J. Am. Chem. Sci. 142 (2020) 5709–5721.
[57] J. Greeley, J.K. Nørskov, Electrochim. Acta 52 (2007) 5829–5836.
[58] X. Wei, S. Wei, S. Cao, Y. Hu, S. Zhou, S. Liu, Z. Wang, X. Lu, Appl. Surf. Sci. 564 (2021) 150423.
[59] A. Muthuperiyanayagam, A.G. Nabi, Q. Zhao, Aman-ur-Rehman, D. Di Tommaso, Phys. Chem. Chem. Phys. 25 (2023) 13429–13441.
[60] I.C. Man, H.Y. Su, F. Calle-Vallejo, H.A. Hansen, J.I. Martínez, N.G. Inoglu, J. Kitchin, T.F. Jaramillo, J.K. Nørskov, J. Rossmeisl, Chem. Cat. Chem. 3 (2011) 1159–1165.
[61] K. Yamasumi, K. Nishimura, Y. Hisamune, Y. Nagae, T. Uchiyama, K. Kamitani, T. Hirai, M. Nishibori, S. Mori, S. Karasawa, T. Kato, K. Furukawa, M. Ishida, H. Furuta, Chem. Eur. J. 23 (2017) 15322–15326.
[62] N. Liu, S. Bartling, A. Springer, C. Kubis, O.S. Bokareva, E. Salaya, J. Sun, Z. Zhang, S. Wohlrab, A.M. Abdel-Mageed, H.-Q. Liang, R. Francke, Adv. Mater. (2023) 2309526.
[63] J. Wang, G. Wang, J. Zhang, Y. Wang, H. Wu, X. Zheng, J. Ding, X. Han, Y. Deng, W. Hu, Angew. Chem. 133 (2021) 7680–7684.
[64] A.G. Nabi, A. Hussain, G.A. Chass, D. Di Tommaso, Nanomater. 13 (2022) 87.
[65] M.D. Higham, M.G. Quesne, C.R.A. Catlow, Dalton Trans. 49 (2020) 8478–8497.
[66] N. Austin, J. Ye, G. Mpourmpakis, Catal. Sci. Technol 7 (2017) 2245–2251.
[67] N. Austin, B. Butina, G. Mpourmpakis, Prog. Nat. Sci. 26 (2016) 487–492.
[68] J. Dean, Y. Yang, N. Austin, G. Veser, G. Mpourmpakis, ChemSusChem. 11 (2018) 1169–1178.
[69] F. Calle Vallejo, M.T. Koper, Angew. Chem. 125 (2013) 7423–7426.
[70] W. Rong, H. Zou, S. Tan, E. Hu, F. Li, C. Tang, H. Dai, S. Wei, Y. Ji, L. Duan, CCS Chem. 5 (2023) 1176–1188.